Journal of Materials Chemistry A

Accepted Manuscript

This article can be cited before page numbers have been issued, to do this please use: M. Wu, Y. Liu, Y. Zhu, L. Jin, J. Liu, H. Hu, Y. Wang, Q. Zhao, R. Lv and J. Qiu, *J. Mater. Chem. A*, 2017, DOI: 10.1039/C7TA03264A.

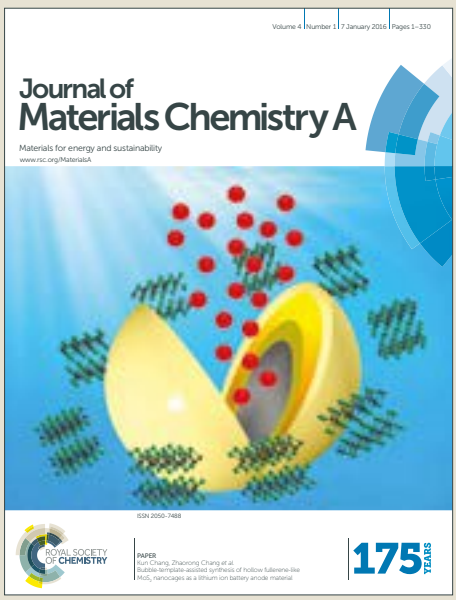

ROYAL SOCIETY OF CHEMISTRY

rsc.li/materials-a

View Article Online
DOI: 10.1039/C7TA03264A

Journal Name

ARTICLE

Supramolecular Polymer-Assisted Synthesis of Nitrogen and Sulfur Dual-Doped Porous Graphene Networks from Petroleum Coke as Efficient Metal-Free Electrocatalysts for Oxygen Reduction Reaction

Received 00th January 20xx,
Accepted 00th January 20xx

DOI: 10.1039/x0xx00000x

www.rsc.org/

Mingbo Wu[a]*, Yang Liu[a], Yulong Zhu[a], Jin Lin[c], Jingyan Liu[a], Han Hu[b], Yang Wang[a], Qingshan Zhao[a], Renqing Lv[c], Jieshan Qiu[b]*

Efficient metal-free carbon electrocatalysts for oxygen reduction reaction (ORR) represent a promising alternative to scarce and price noble-metal-based counterparts while their performance remains to be significantly boosted to fulfill the requirement of the real application. Herein, the rational design and synthesis of nitrogen and sulfur co-doped porous graphene networks (N,S-PGN) is present for highly efficient ORR. With the assistance of superamolecular polymers, petroleum coke, a byproduct of oil refinery in million tons per year, can be converted into N,S co-doped graphene nanosheets with a highly porous architecture. Such a hierarchical and doped structure would allow high expose of active sites and facilitate the electron transport. As a result, the N,S-PGN exhibits remarkable electrocatalytic activities for ORR and in particular outperform Pt/C electrode in terms of superior diffusion-limiting current density and stability operated under the same condition. Furthermore, the increased carbon active sites and facile electrons transport are confirmed by theoretical calculations where the dual-doping in porous graphene increases the high charge densities of carbon active sites and HOMO energy for ORR. The present work demonstrates a novel and feasible route for preparing heteroatoms co-doped porous graphene for energy-related applications as well as a new strategy for value-added utilization of petroleum coke.

Introduction

The sluggish kinetics of oxygen reduction reaction (ORR) at the cathode of fuel cells requires the use of a significant amount of Pt-based electrocatalysts.[1,2] Nevertheless, the limited availability and prohibitive cost of this noble metal dramatically hinder the wide-spread application of fuel cells.[3-5] On the other hand, the Pt-based electrocatalysts usually suffer from poor stability and tolerance to crossover effect, contributing to the loss of performance during operation.[6-10] As a result, it's highly desirable to rationally design and synthesize low-cost and efficient electrocatalysts for ORR using earth abundant materials.[11-15]

Among all the available non-noble metal ORR electrocatalysts, carbon-based materials stand out because of their great abundance, low price, and high ORR catalytic activities.[16-19] Graphene, a single-atom-thick sheet with two-dimensional structure, has attracted great attention due to its superior electrical conductivity, structural flexibility, and chemical stability *etc.*. Undoubtedly, these unique properties endow graphene a promising platform for electrocatalysis application.[20-22] Moreover, tremendous works have verified that heteroatoms doping is an effective way to tailor the chemical property of graphene. The synergetic effect between heteroatoms and nearby carbon atoms would be a great contributions to enhanced functions.[20-25] Specifically, the redistributions of atomic charge and spin density after heteroatoms doping can equilibrate adsorption and desorption energies of the intermediates in ORR process. Besides, the topological defects generated from heteroatoms doping can act as additional active sites for ORR.[20-24] To strengthen the effects of heteroatoms doping, dual-doping strategies are usually applied. However, most present synthesis methods of dual-doped graphene materials involve laborious procedures and/or toxic and expensive precursors.[26,27]

On the other hand, the intrinsically strong π-π interactions between graphene nanosheets usually induce their restacking, thus seriously hampering the diffusion of electrolyte to the active sites as well as decreasing the exposed reactive edges on the surface and/or defects for efficient adsorption and reduction of oxygen molecules.[28-34] To address this issue, many strategies have been employed to construct graphene-based

[a] State Key Laboratory of Heavy Oil Processing, China University of Petroleum, Qingdao 266580, China;
[b] Carbon Research Laboratory, State Key Lab of Fine Chemicals, School of Chemical Engineering, Dalian University of Technology, Dalian 116024, China;
[c] College of Science, China University of Petroleum, Qingdao 266580, China.

†Electronic Supplementary Information (ESI) available: [details of any supplementary information available should be included here]. See DOI: 10.1039/x0xx00000x

View Article Online
DOI: 10.1039/C7TA03264A

materials with high porosity. Hard-templating methods represent the most straightfoward one, where the templates can be varied from dry ice[35] to silica[20] and metal oxide.[21] Despite the diversity in choosing available templates, the laborious multi-step procedures hinder their widespread implementation.

To address the aforementioned synthesis difficulties, we report a novel superamolecular polymer-mediated synthesis of nitrogen, sulfur-codoped porous graphene networks (N,S-PGN) from petroleum coke (PC). The supramolecular polymer in-situ formed on the PC-derived graphene nanosheets through polymerization of melamine and trithiocyanuric acid (MT for short) can not only serve as the precursors for heteroatoms doping, but also acts as compartment to prevent the aggregation of graphene nanosheets, leading to porous architecture. Benefiting from the compositional and structural advantages, N,S-PGN affords remarkable ORR performance in terms of extremely positive onset potential, preferable limiting current density (-7.2 mA cm^{-2}) and excellent long-term durability in alkaline environment, comparable favorably to the benchmark ORR catalysts Pt/C. The underlying mechanism behind this remarkable ORR activity is further elucidated by theoretical calculations. The present work makes a significant contribution to the design and synthesis of graphene-based materials with desirable architectures for electrocatalysis applications as well as a reliable strategy for value-added utilization of PC.

Experimental

Materials and methods

PCGO was prepared by a modified Hummers and Offeman's method using petroleum coke (PC for short, contains 97.14% C and 2.86% H detected by Elemental Analyzer) from SINOPEC, China as the precursor.

In a typical synthesis, 2 g PC powder, 1.6 g $NaNO_3$, and 100 mL of 98% H_2SO_4 were first mixed in a flask located in an ice bath. Then, 10 g $KMnO_4$ was slowly added under vigorous agitation. After that, the mixture was kept at 5 ^oC under gentle stirring for 48 h to produce a highly viscous slurry. Subsequently, the flask was transferred into a 35 ± 5 ^oC water bath and the mixture continued to be stirred for another 48 h until a dark brown thick paste was formed. 200 mL deionized (DI) water was then added dropwise, and the resultant dispersion was kept for 1 h while the temperature was raised to 95 ± 5 ^oC before 100 mL water was added. Following that, 50 mL H_2O_2 (30%) was slowly added to reduce the insoluble manganese species. The PCGO were then purified by repeatedly washing with DI water to remove all the unwanted ions. The mixture was allowed to stand overnight for settlement and washed with 5% HCl aqueous solution (500 mL) to remove metal ions. The sample was then washed with DI water until pH ~7. Exfoliation was carried out by sonicating the suspension for 96 h. Low-speed centrifugation was done at 4000 rpm for 4 min until all visible particles were removed (repeat 3-5 times) from the precipitates. The supernatant then underwent high-speed centrifugation at 8000 rpm for 35 min to collect PCGO nanosheet and water-soluble products. Freeze dried final sediment for further use.

80 mg PCGO was dispersed in 80 mL DI water by ultrasonication for 3 h. Then, 168 mg (112 mg, 224 mg) melamine was dissolved in the GO dispersion under stirring at 80 °C. Afterward, 249 mg (166 mg, 332 mg) trithiocyanuric acid was added into the mixture and further stirred at 80 °C for 1 h. The obtained dispersion was then transferred to a Teflon-lined stainless steel autoclave (90 mL in capacity) and heated in an oil bath at 100 ^oC for 4 h. During the hydrothermal process, the system should be mildly stirred (350 rpm). After cooling down to room temperature naturally, the as-obtained mixture was filtered and washed several times with DI water, and freeze dried to obtain MT@PCGO (MT@PCGO-r1, MT@PCGO-r2).

The MT@PCGO was annealed in N_2 atmosphere at a flow of 60 cm^3 min^{-1} with a heating rate of 5 °C min^{-1} to final pyrolysis temperature (700, 800, and 900 °C) for 2 h to obtain N,S-PGN-t (tempereture). For comparsion, N-G-800 (without trithiocyanuric acid), T-G-800 (without melamine) and PCGO-800 (without either trithiocyanuric acid or melamine) were also prepared by thermal treatment of their precursor under the same condition. Besides, the mixture of melamine, trithiocyanuric acid and PCGO were grinded, and then calcined at 800 ^oC to obtain N,S-G. The calcination of MT@PCGO-r1 and MT@PCGO-r2 at 800 ^oC to were aimed to get N,S-PGN-800r1 and N,S-PGN-800r2 respectivly.

Characterizations of the Samples

The morphology of the samples was investigated by a JSM 7401F (JEOL Ltd., Tokyo, Japan) scanning electron microscope (SEM) operated at 3.0 kV and a JEM 2010 (JEOL Ltd., Tokyo, Japan) transmission electron microscope (TEM) operated at 120.0 kV. X-ray photoelectron spectroscopic (XPS) measurements were performed on a VG Microtech ESCA 2000 using a monochromic Al X-ray source (97.9 W, 93.9 eV). X-ray diffraction (XRD) patterns were recorded on a Miniflex Desktop X-ray Diffractometer. Fourier transform infrared spectra (FITR) were detected on a PerkinElmer spectrum GX FTIR system. The Raman spectra were collected on a (Renishaw) Raman spectrometer using 514 nm laser. The pore structure was investigated by nitrogen adsorption-desorption isotherms on a sorptometer (Micromeritics, ASAP 2020, America).

Computational methods

All structures of samples were optimized and the electronic properties were calculated by density functional theory (DFT) at B3LYP/6-31G+ (d, p) level (for radical structures, UB3LYP was used) through Gaussian 09.

Electrochemical measurements

The working electrode was prepared as follows: 2 mg N,S-PGN was dispersed in a solvent mixture of 5 wt% Nafion solution (0.005 mL) and ethanol (0.8 mL) under sonication for 1 h. Then, 15 µL of the suspension was pipetted onto the glassy-carbon disk electrode and dried in air. Electrochemical measurements including cyclic voltammetry, linear sweep voltammetry and cycling ability were performed on an electrochemical workstation (CHI 760E, CH Instrument, China) equipped with a three-electrode cell system. The glass carbon rotating disk electrode loaded with electrocatalyst was used as the working electrode, an Ag/AgCl electrode as the reference electrode, and a Pt wire as the counter electrode. ORR test was carried out in an O_2 saturated 0.1 M KOH aqueous solution (70 mL). For the durability test of methanol, 47.5 µL methanol dissolved in 1 mL 0.1 M KOH was added to the O_2 saturated 0.1 M

View Article Online
DOI: 10.1039/C7TA03264A

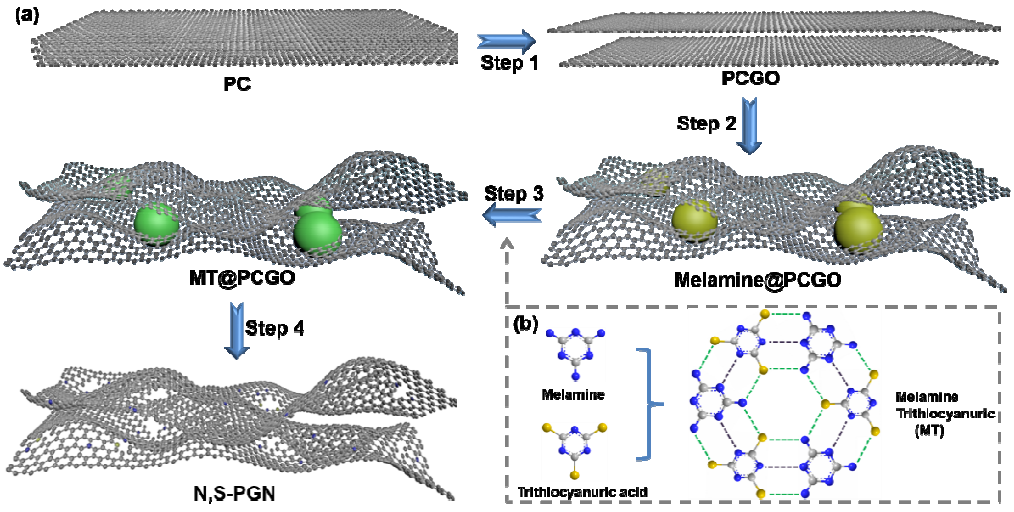

Figure 1. (a) Schematic illustration of the synthesis procedure of N,S-PGN materials. Step 1: PCGO was obtained from PC via modified Hummers and Offeman's method. Step 2: Melamine was dissolved in PCGO solution at 80 ^{o}C; Step 3: Supramolecular polymerization of melamine and trithiocyanuric acid proceeded in PCGO layers; Step 4: Thermal treatment of MT@PCGO in N_2. (b) Supramolecular polymerization of melamine and trithiocyanuric acid results in the formation of MT.

KOH aqueous solution around 300 s, and the current was collected at -0.4 V vs. Ag/AgCl with a rotation speed of 1600 rpm. The Koutecky-Levich plots were obtained by linear fitting of the reciprocal rotating speed versus reciprocal current density collected at different potentials from -0.4 V to -0.75 V. The overall electron transfer numbers per oxygen molecule involved in a typical ORR werecalculated from the slopes of Koutecky-Levich plots by the following equation:

$1/j_D = 1/j_k + 1/B\omega^{1/2}$

where j_k is the kinetic current in ampere at a constant potential, ω is the electrode rotating speed in rpm, and B, the reciprocal of the slope, which was determined from the slope of Koutecky-Levich plots based on Levich equation as followed:

$B= 0.2\ nFA\nu^{-1/6}Co_2Do_2^{2/3}$

where n is the number of electrons transferred per oxygen molecule, F is the Faraday constant (96485 C mol^{-1}), Do_2 is the diffusion coefficient of O_2 in 0.1 M KOH (1.9×10^{-5} cm s^{-1}), ν is the kinetic viscosity, and Co_2 is the concentration of O_2 (1.2×10^{-3} mol L^{-1}). The constant 0.2 is adopted when the rotating speed is in rpm. The electron transfer number n was calculated based on the disk (I_d) and ring current (I_r) as follows: $n=4I_d/(I_d+I_r/N)$, where N is current collection efficiency of the Pt ring (0.43).

Results and discussion

The fabrication process of N,S-PGN is explicitly illustrated in Figure 1. Firstly, melamine was dissolved in the petroleum coke based graphene oxide (PCGO) dispersion and the π-π interaction permits the adsorption of melamine on the surface of PCGO.[36] Then, the trithiocyanuric acid was added into the mixture to induce a supramolecular polymerization between melamine and trithiocyanuric acid, contributing to the formation of Melamine Trithiocyanuric nanocrystals and PCGO composites (denoted as MT@PCGO) under stirring. Subsequently, themal treatment was applied during which the MT nanocrystals would decompose to release N- and S-containing species to drive the heteroatom doping. Meanwhile, the pre-introduction of these nanoscrystals on the surface of PCGO inhibited the restacking of graphene nanosheets during carbonization, giving rise to highly porous structures. As a result, more active sites are supposed to be created and exposed.[37,38]

As a cheap and abundant byproduct of oil refinery, petroleum coke (PC) with high graphitization was explored as the precursor of graphene. The sharp (002) peak of graphitic plane (at around 25.3^{o}) shown in XRD pattern (Figure S1) and remarkable G and 2D band appeared[26] in Raman spectra (Figure S2) verify the great possibility of PC to be fully exfoliated.[39-43] XRD pattern of PCGO (Figure S1) shows a characteristic diffraction peak located at $2\vartheta = 11.2^{o}$ with an interlayer spacing of 0.79 nm, which is assigned to the expanded (002) plane due to the intercalation of oxygen functional groups between the graphene layers. The Raman spectrum (Figure S2) of PCGO affords the typical D peak (1350 cm^{-1}), G peak (1590 cm^{-1}), 2D peak (2698 cm^{-1}) with an I_D/I_G intensity ratio of 0.84, confirming lattice distortions induced by oxidation.[39] Meanwhile, obviously layered flakes detected from the TEM images (Figure S3a,S3b) can further prove the formation of PCGO.

To evaluate the efficency of proposed strategy and disclose the correlation between the electrocatalytic performance and microstructure of as-obtained materials, systematic characterizations were performed. Supramolecules nanocrystals decorated on PCGO nanosheets possess a small size of around 50-100 nm (Figure 2a) without difference compared with counterpart in MT@GO (Figure S4a) from natural graphite while the crystals would grow into several tens of micrometers without the involvement of PGCO (Figure S4b), implying the π-π interaction between PCGO and melamine are beneficial to form ultrafine crystals that are ready to be dispersed among graphene nanosheets. Remarkably, subsequent pyrolysis of MT@PCGO leads to the formation of distinct porous graphene networks at the

View Article Online
DOI: 10.1039/C7TA03264A

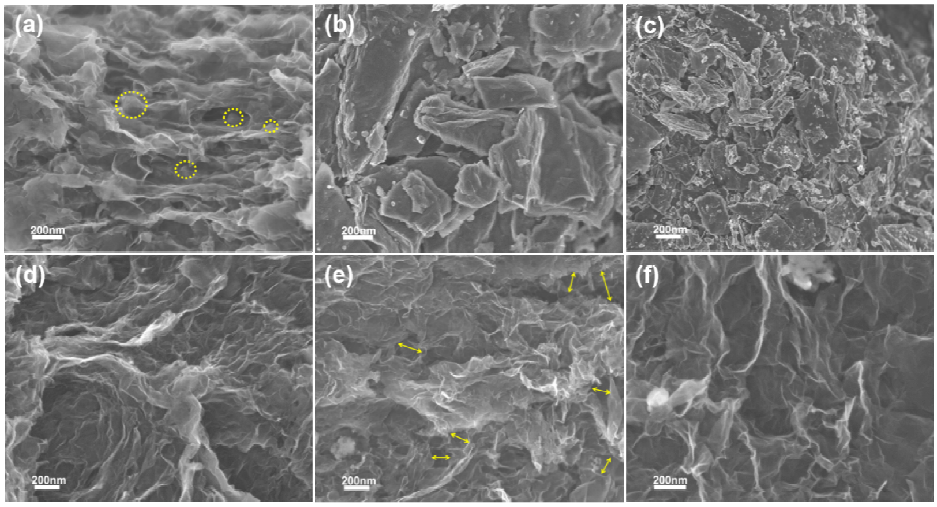

Figure 2. FESEM images of (a) MT@PCGO, (b) PCGO-800, (c) N,S-G-800, (d) N,S-PGN-700, (e) N,S-PGN-800 and (f) N,S-PGN-900.

elevated temperature. The graphene networks formed at 700, 800, and 900 ^{o}C all exhibit crumpled and loose-packed structure where the fluffy graphene nanosheets are overlapped on and interconnected among each other as shown in Figure 2d-2f. The porosity of N,S-PGN with diameters ranging from submicrometer to several nanometers is similar to that of freeze-dried graphene aerogels,[42,43] while differs from that of the thermally reduced PCGO (PCGO-800), which presents a typical densely aggregated graphite-like bulks prepared without MT (Figure 2b). To demonstrate the role of in-situ formed MT nanocrystals on the formation of porous structures, the same heating process was applied on the physical mixture of MT microcrystals and PCGO. As shown, the absence of visible pores demonstrates the significant role of polymer MT on effectively preventing the restacking of graphene nanosheets and expediting the formation of pores (Figure 2c). Large amounts of transparent porous graphene networks after decomposition of MT can also be readily observed, and the surface of the graphene nanosheets under TEM observations (Figure 3a,3b) is highly wrinkled, indicating the high degree of defect which may be induced through the heteroatoms doping. The HRTEM image shows cavity on the surface of these nanosheets which may facilitate the expose of active sites.[22,44,45] Moreover, the EDS mappings (Figure 3d-3f) indicate a homogeneous distribution of C, N, and S in the as-obtained N,S-PGN.

The porosity of N,S-PGNs were further evaluated by nitrogen adsorption-desorption techniques (Figure 4). The typical type-IV isotherms and obvious H_3 type hysteresis loop indicate the abundance of mesopores of N,S-PGNs, which is consistent with the morphology shown in SEM and TEM images,[46,47] and the related parameters are summarized in Table 1. Apparently, it can be easily found that the BET surface area and pore diameter of the N,S-PGNs are larger than those of PCGO-800, which is regularly dependent on the pyrolysis temperature. In particular, the BET surface area decreases from 571 to 425 $m^2 \cdot g^{-1}$ while the average pore size increases from 14 to 18 nm with the carbonization temperature rising from 700 to 900 ^{o}C, and total pore volume remains almost unchanged, which may be associated with the introduction of MT. Furthermore, the higher surface area and larger pore volume of the N,S-PGN compared to those of PCGO-800 demonstrates that the MT polymer be served as an efficient template to protect the architecture of graphene from collapsing, resulting in ultrathin graphene layers with a mesoporous networks scaffold.[37,38] On the other hand, the in-situ released gas from MT decomposition can generate more pores and random edge sites. High surface area, large volume, and plentiful topological defects can not only facilitate the accessibility of electrolyte and diffusion of reactants, but also provide additional active sites for ORR.[20-25]

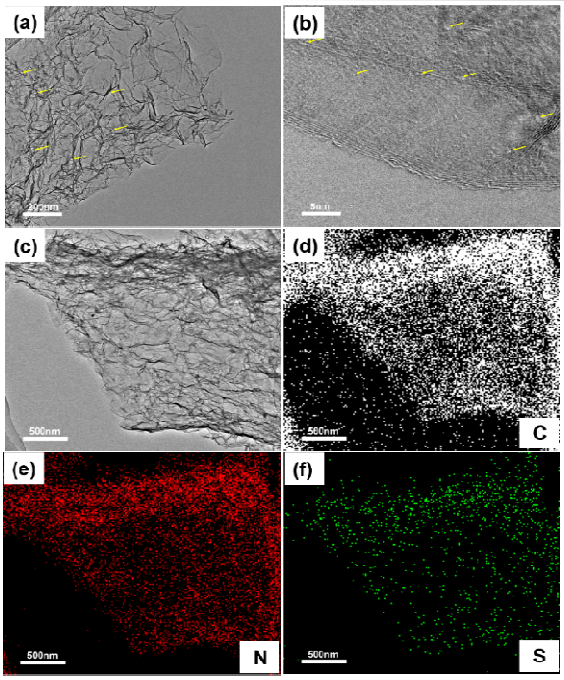

Figure 3. (a) TEM and (b, c) HRTEM images of N,S-PGN-800. (d-f) EDS mapping image of N,S-PGN-800 with the corresponding element.

View Article Online
DOI: 10.1039/C7TA03264A

Journal Name

ARTICLE

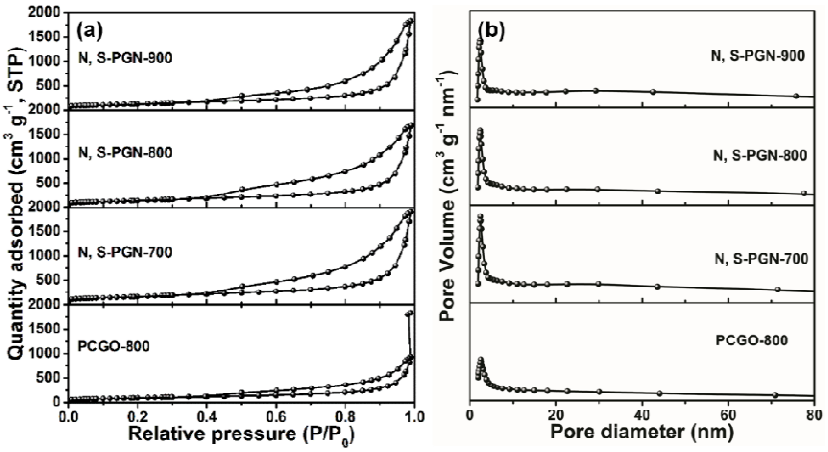

Figure 4. (a) Nitrogen adsorption-desorption isotherms and (b) The corresponding pore size distribution of all N,S-PGN samples and PCGO-800.

Table 1. The nitrogen adsorption-desorption parameters of all N,S-PGN materials and PCGO-800.

Samples	S_{BET} ($m^2 \cdot g^{-1}$)	S_{Lang} ($m^2 \cdot g^{-1}$)	V_{micro} ($cm^3 \cdot g^{-1}$)	S_{micro} ($m^2 \cdot g^{-1}$)	V_{tot} ($cm^3 \cdot g^{-1}$)	D_{av} (nm)
PCGO-800	314	499	0.11	255	0.97	12
N,S-PGN-700	571	815	0.19	458	2.1	14
N,S-PGN-800	486	651	0.16	389	1.9	16
N,S-PGN-900	425	564	0.14	346	1.9	18

XPS spectras were employed to analysis the state of the heteroatoms in the N,S-PGNs (Figure 5a). The content of heteroatoms in different samples is presented in Table S1 (Supporting Information). As shown in Figure 5b and Figure S5, the XPS N 1s spectrum can be fitted to three component peaks centered at 398.4, 399.8 and 401.3 eV, attributing to pyridinic, pyrrolic, and graphitic N species, respectively, among which the pyridine-like N is the primary N species in N,S-PGNs. These characteristics are accorded with the subsequent theoretical calculations, which have demonstrated that the pyridine-like N is mostly favorable for fast transportation of mass and charge, as well electrochemical reaction.[22-24] In addition, the high resolution of S 2p peaks are also deconvoluted into three peaks associated with C–S–C (163.2 eV for S $2p_{3/2}$ and 164.4 eV for S $2p_{1/2}$) and C–SO_x–C (167.8 eV) species (Figure 5c), further confirming that MT polymers simultaneously serve as N- and S- precursors. These heteroatoms can change the atomics charge/ defects distributions of the graphene matrix, are supposed to enhance electrocatalytic activity.[7-11]

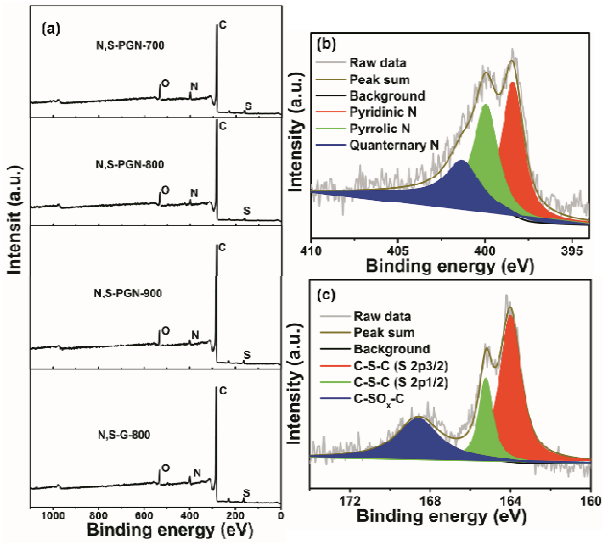

Figure 5. (a) XPS survey spectra of all N,S-PGN samples and N,S-G-800. High resolution (b) N1s and (c) S2p XPS spectra of N,S-PGN-800.

View Article Online
DOI: 10.1039/C7TA03264A

Journal Name

ARTICLE

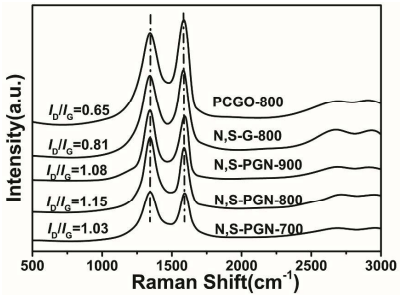

Figure 6. Raman spectra of N,S-PGN samples, N,S-G-800 and PCGO-800.

The structural defects on N,S-PGNs can be further confirmed from XRD and Raman spectroscopies. As illustrated in Figure S6, the diffraction peak at 11.2° shifts to 26.2° after the removal of oxygen-containing functional groups from graphene sheets of PCGO by pyrolyzing at 800 °C, corresponding to the decreasing of interlayer spacing from 0.79 of 0.34 nm.[46-48] It is worth noting that PCGO-800 presents a well-defined peak while N,S-PGN displays a broad hump-shaped peak, which further verifies the disordered and defective graphene nanosheets were generated with the assistant of MT in N,S-PGNs. In addition, the characteristic peaks at around 1355 cm^{-1} (D-band) and 1600 cm^{-1} (G-band) in Raman spectra are associated with the defects in the graphene and the planar motion of sp^2-hybridized carbon atoms in graphene layers, respectively.[49-52] The considerable amount of disordered moieties and edge defects introduced by N, S co-doping can be confirmed by Raman spectra (Figure 6).[20-24] The highest I_D/I_G intensity ratio of N,S-PGN-800 implies that there are more defects in graphene layers compared with other references, which may afford the highest activity for ORR.[53,54]

Considering the high N and S contents, porous networks, large S_{BET} and defects riched property of N,S-PGNs, superior electrocatalytic performances for ORR were expexted. The electrocatalytic activity was primarily evaluated through cyclic voltammetry (CV) (Figure 7a).in 0.1 M KOH electrolyte with Pt wire and Ag/AgCl as the counter electrode and reference electrode, respectively. A CV curve without any obvious redox peak was obtained when the electrolyte was saturated with inert Ar, as a result of the typical supercapacitance effect on porous carbon materials.[53,54] In contrast, when O_2 was introduced, a well-defined characteristic ORR peak, centering at -0.18 V along with a peak current density of -3.2 mA cm^{-2} was observed, slightly negative than that of commercial Pt/C electrocatalyst (centering at -0.15 V with a peak current density of -1.5 mA cm^{-2}, Figure S7), and superior to that of N,S-PGN-700 (centering at -0.18 V with a peak current density of -1.9 mA cm^{-2}, Figure S8) and N,S-PGN-900 (centering at -0.21 V with a peak current density of -1.9 mA cm^{-2}, Figure S9). Moreover, the reduction peak potential for N,S-PGN-800 is also more positive than that of many recently reported metal-free ORR catalysts, such as N,S-graphene,[20,44] N,S-carbon nanosheets,[17] and N-graphene/carbon,[55,56] indicating a superior ORR activity.

The ORR performance of N,S-PGNs were further evaluated through linear sweep voltammogram (LSV) measurements. The onset potentials (E_{onset}) and half-wave potential ($E_{1/2}$) for N,S-PGN-700 (-0.04 V, -0.149 V), N,S-PGN-800 (-0.04 V, -0.145 V), and N,S-PGN-900 (-0.04 V, -0.147 V) as illustrated in Figure 7b are comparable to those of commercial Pt/C (-0.03 V, -0.125 V) catalyst apart from negligibly more negative potentials. Meanwhile, a superior diffusion-limiting current density for N,S-PGN-800 of 7.2 mA cm^{-2} was obtained, comparable favorably to 6.4 mA cm^{-2} of Pt/C. This high current density of N,S-PGN-800 also prevails over most reported metal-free electrocatalysts.[21-25] Obviously, M-G-800 and T-G-800 possess extremely unsatisfactory electrochemical behaviour due to the lack of synergistic effects for N, S co-doping. Besides, although N,S-G-800

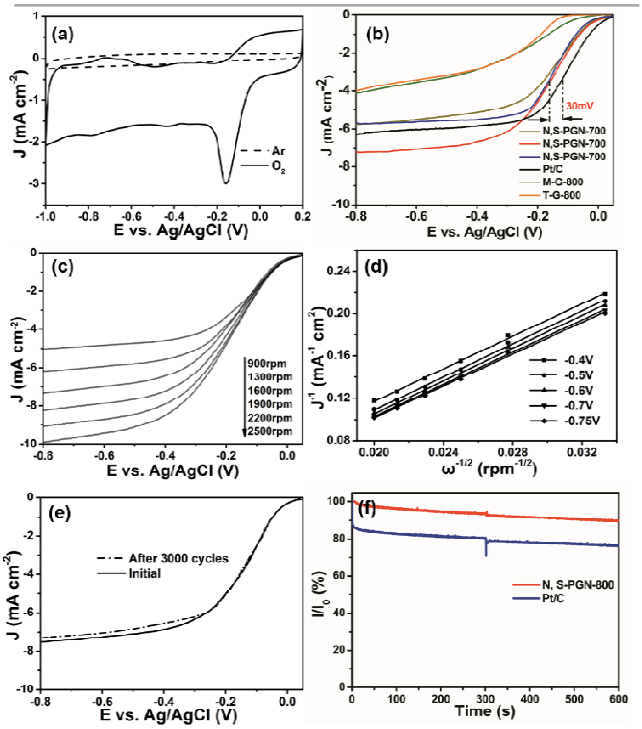

Figure 7. (a) CV curves of N,S-PGN-800 in Ar and O_2 saturated 0.1 M KOH aqueous solution with a scan rate of 10 mV s^{-1}. (b) LSV curves of all N,S-PGN materials, M-G-800, T-G-800 and Pt/C in O_2-saturated 0.1 M KOH electrolyte with a 5 mV s^{-1} and a rotation rate of 1600 rpm. (c) LSV curves of N,S-PGN-800 at different rotation rates. (d) K-L plots at different potentials based on the results of (c). (e) LSV curves of N,S-PGN-800 before and after cycling for 3000 cycles with a rotation rate of 1600 rmp. (f) The durability test of N,S-PGN-800 and Pt/C for methanol.

View Article Online
DOI: 10.1039/C7TA03264A

Journal Name

ARTICLE

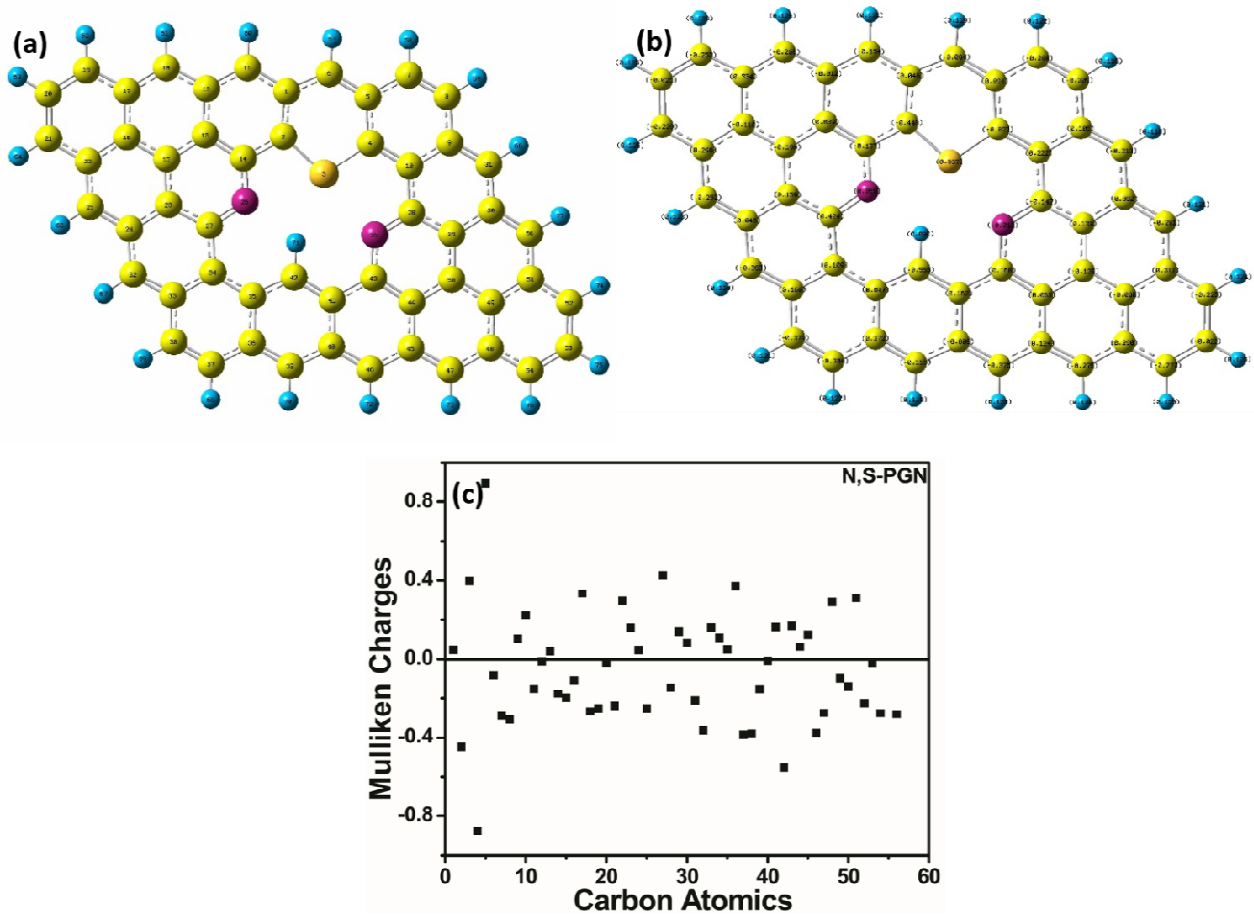

Figure 8. (a)Atomic order and (b) Mulliken charges distribution on N,S-PGN models. Yellow is carbon, orange is sulfur, and purple is nitrogen. (c) Mulliken charges of carbon atomics in N,S-PGN models.

(Figure S10b) share similar co-doping synergy with N,S-PGN-800, but delivers inferior catalytic activities. Thus, the electrocatalytic activities not only originate from the dual heteroatoms dopants, but also largely depend on the sufficiently exposed active sites arising from the microstructure and pore-induced defective segment.

The Koutechy-Levich (K-L) analysis was performed to qualify the ORR process on this novel catalyst by rotating disk electrode (RDE) measurement at various rotating speeds (Figure 7c). K-L plots (J^{-1} vs $\omega^{-1/2}$) of N,S-PGN-800 were derived from the LSV curves, which represent the correlation between inverse current density (J^{-1}) and the inverse of the square root of rotation speed ($\omega^{-1/2}$) (Figure 7d). Good linearity of K–L plots is observed, revealing the first-order oxygen.[24-28] Furthermore, electron transfer numbers (n) of N,S-PGN-800 determined from the slopes of linear K-L plots and RRDE calculation results (Figure S11) are 3.9-4.0, similar to ~4.0 of Pt/C electrocatalyst, suggesting its perfect selectivity for the efficient four-electron-dominated ORR pathway.[29-32]

In addition, the N,S-PGN-700 and N,S-PGN-900 also possess the comparable electron transfer numbers, revealing different reaction pathways and strongly supporting the existence of synergism between N, S co-doping and porous network framework of N,S-PGN. More evidences to support this hypothesis were found in the kinetic current densities determined by the intercepts of K-L plots. The current densities at -0.6 V increase in the order: N,S-PGN-700 < Pt/C < N,S-PGN-900 < N,S-PGN-800 (11.6, 13.7, 14.2 to 23.6 mA cm^{-2}). Moreover, N,S-PGN-800 exhibits excellent electrochemical performance in terms of superior Tafel slope (123 mV dec^{-1}, Figure S12) in comparison with Pt/C (125 mV dec^{-1}), suggesting that the transfer of the first electron is the rate-determining step in the ORR process for N,S-PGN. As a result, a facilitated reactant diffusion

View Article Online
DOI: 10.1039/C7TA03264A

Journal Name

ARTICLE

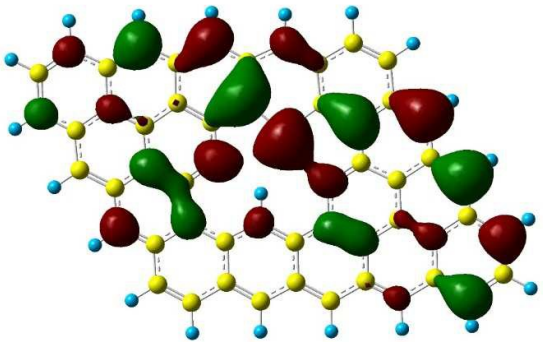

Figure 9. HOMO distribution on N,S-PGN configurations.

Table 2. HOMO energy level on N,S-PGN and other referential configurations.

Catalysts	HOMO energy/ Hartree[a)]
N-G	-0.16301
S-G	-0.25479
N,S-PGN	-0.16280
G	-0.16312
PG	-0.15104

[a)]1 hartree = 27.21 eV = 627.51 kcal/mol =2625.5 kJ/mol

between active sites in the N,S-PGN can be expected due to the large S_{BET}, and highly porous network.[55,56] N,S-PGN-800 also exhibits superior electrochemical stability (Figure 7e and Figure S13) and tolerance to methanol-crossover effects (Figure 7f) to the commercial Pt/C electrocatalyst. It is believed that the proper heteroatoms co-doping level and microstructure of N,S-PGN-800 are responsible for this enhanced durability and resistance to poisoning.

On the basis of structure-property correlation, the outstanding ORR electrocatalytic activities of N,S-PGN-800 should originate from its sufficient defects and active centers created by heteroatoms co-doping as well as the unique porous architecture. The co-doping of N and S could synergistically modulate the catalytic sites and local electronic structure of graphene materials, leading to enhanced ORR activity. In addition, the unique porous structure of N,S-PGN with corrugated and interconnected morphology has been confirmed to provide more exposure of active sites, as well a facilitated pathway for the facile transport of reactants and products associated with the electrochemical reactions (e.g. the access of O_2 in ORR). The aforementioned characteristics and the electrocatalytic performance of all N,S-PGNs are summarized in Table S1. As shown, the N,S-PGN-800 possesses the highest defects and best electrocatalytic performance, indicating the appropriate N, S co-doping degree (relate to calcinated temperature) coupled with unique porous morphology can synergistically enhance the electrocatalytic activity of ORR.

The electron configurations of nitrogen and sulfur codoped porous graphene networks for remarkable ORR performance were further calculated and revealed by density functional theory (DFT) calculation, which were carried out to study synergistic effects of pyridine-type N and S in simplified model based XPS results (Figure 8a,b). Pristine graphene, porous graphene and graphene doped with sole N or S atom models have been constructed for referential experiments as shown in Figure S14-S17. Previous works illustrated that the carbon atoms with decreased Mulliken charges surrounded by heteroatoms and defects moiety are supposed to be catalytic active sites of ORR, and the number of this type of carbon atoms could also be regarded as an index to estimate the electrocatalytic performance for ORR.[21-25] As shown in Figure 8c, a maximum number and charge densities of active carbon sites in N,S-PGN model are dramatically increased attributing to the regulation of atomic charge density by heteroatoms co-doping compared with other models (in Figure S18). In addition, we calculated the highest occupied molecular orbital (HOMO) distributions on all graphene models (Figure 9 and Figure S19), which represents potential of electron donor.[29-33] The state of the orbital distributions is related to the electron transfer during the ORR. Interestingly, P-G model possesses highest HOMO energy level and N,S-PGN secondly (Table 2), indicating that both can give rise to more electrons to accelerate the reduction of dissolved O_2. But there were less active carbon sites and extremely lower Mulliken charges density in P-G compared with N,S-PGN model (in Figure 9). Combined with the abovementioned results, we can draw a conclusion that excellent ORR catalytic performance on N,S-PGN may be derived from the synergy among the HOMO energies of models, maximum number and charge densities of active carbon sites. This synergetic feature can suitably explain the underlying mechanism of N and S co-doping in enhancing ORR catalytic performance.

Conclusions

In summary, we have reported the supramolecular polymer-mediated synthesis of N,S-PGNs from PC for efficient ORR. The supramolecular polymer in-situ formed on the surface of the graphene nanosheets can simultaneously serve as sources of heteroatoms and prevent the restacking of graphene nanosheets through intrinsically strong π-π interaction. The resulted graphene nanosheets show large surface area, high porosity, and large amount of heteroatoms including N and S. These structural merits works synergistically, allowing the N,S-PGNs to afford outstanding performance towards ORR, which is comparable favorably to the benchmark Pt/C electrocatalyst.

View Article Online
DOI: 10.1039/C7TA03264A

Furthermore, the synergistic effects of the N,S-PGNs for ORR have been carefully probed by comparing graphene nanostructures synthesized under different conditions as well as through DFT calculation. This facile supramolecular polymer-assisted synthesis strategy will pave the way for the targeted design and fabrication of advanced metal-free carbon electracatalysts for ORR and other applications. Meanwhile, this fantastic strategy realizes the value-added utilization of petroleum coke.

Acknowledgements

This work was supported by the National Natural Science Foundation of China (Nos. 51372277, 51572296, U1662113); the Fundamental Research Fund for the Central Universities (No. 15CX08005A).

Notes and references

1 M. Armand and J. M. Tarascon, *Nature*, 2008, **451**, 652.
2 M. K. Debe, *Nature*, 2012, **486**, 43.
3 C. L. Tan and H. Zhang, *Nat. Commun*., 2015, **6**, 1.
4 L. Z. Bu, J. B. Ding, S. J. Guo, X. Zhang, D. Su, X. Zhu, J. L. Yao, J. Guo, G. Lu and X. Q. Huang, *Adv. Mater.*, 2015, **44**, 7204.
5 J. B. Wu and H. Yang, *Acc. Chem. Res*., 2013, **46**, 1848.
6 L. Ma, C. M. Wang, B. Y. Xia, K. K. Mao, J. W. He, X. J. Wu, Y. J. Xiong, X. W. Lou, *Angew. Chem. Int. Ed.,* 2015, **19**, 5666.
7 L. Grande, E. Paillard, J. Hassoun, J.B. Park, Y.J. Lee, Y. K. Sun, S. Passerini and B. Scrosati, *Adv. Mater.*, 2015, 27, 784.
8 Q. Li, R. G. Cao, J. Cho and G. Wu, *Adv. Energy Mater.*, 2014, **4**, 1301415.
9 Z. Zhu, Y. Yan, Y. Guan, J. H. Xue and L. L. Cui, *J. Mater. Chem. A*, 2016, **4**, 15536.
10 G. Wu and P. Zelenay, Acc*. Chem. Res.*, 2013, **46**, 1878.
11 Y. Zheng, Y. Jiao, L. Ge, M. Jaroniec and S. Z. Qiao, *Angew. Chem. Int. Ed.*, 2013, **113**, 192.
12 Y. Nie, L. Li and Z. D. Wei, *Chem.Soc. Rev.,* 2015, **44**, 2168.
13 S. Zhang, X. Zhang, G. M. Jiang, H. Y. Zhu, S. J. Guo, D. Su, G. Lu and S. H. Sun, *J. Am. Chem.*, Soc. 2014, **136**, 7734.
14 L. Shang, H. J. Yu, X. Huang, T. Bian, R. Shi, Y. F. Zhao, G. I. N. Waterhouse, L. Z. Wu, C. H. Tung and T. R. Zhang, *Adv. Mater*., 2016, **28**, 1668.
15 Y. Z. Su, Z. Q. Yao, F. Zhang, H. Wang, Z. Mics, E. Canovas, M. Bonn, X. D. Zhuang, X. L. Feng, *Adv. Funct. Mater.*, 2016, **26**, 5893.
16 S. H. Liu, Y. F. Dong, C. T. Zhao, Z. B. Zhao, C. Yu, Z. Y. Wang and J. S. Qiu, *Nano Energy*, 2015, **12**, 578.
17 J. T. Zhang, L. T. Qu, G. Q. Shi, J. Y. Liu, J. F. Chen and L. M. Dai, *Angew. Chem. Int. Ed*., 2016, **128**, 2270.
18 K. G. Qu, Y. Zheng, S. Dai and S. Z. Qiao, *Nano Energy*, 2016, **19**, 373.
19 J. T. Zhang, Z. H. Zhao, Z. H. Xiao and L. M. Dai, *Nat. Nanotechnol.*, 2015, **10**, 444.
20 X. Gong, S. S. Liu, C. Y. Ouyang, P. Strasser and R. Z. Yang, *ACS Catal.*, 2015, **5**, 920.
21 J. Liang, Y. Jiao, M. Jaroniec and S. Z. Qiao, *Angew. Chem. Int. Ed.*, 2012, **51**, 11496.
22 C. Tang, H. F. Wang, X. Chen, B. Q. Li, T. Z. Hou, B. S. Zhang, Q. Zhang, M. M. Titirici and F. Wei, *Adv. Mater.*, 2016, **28**, 6845.
23 Y. Jiao, Y. Zheng, M. Jaroniec and S. Z. Qiao, *J. Am. Chem. Soc.*, 2014, **136**, 4394.
24 W. H. Niu, L. G. Li, X. J. Liu, N. Wang, J. Liu, W. J. Zhou, Z. H. Tang and S. W. Chen, *J. Am. Chem. Soc.*, 2015, **137**, 5555.
25 Y. Zheng, Y. Jiao, L. Ge, M. Jaroniec and S. Z. Qiao, *Angew. Chem. Int. Ed.*, 2013, **125**, 3192.
26 Y. Jia, L. Z. Zhang, A. J. Du, G. P. Gao, J. Chen, X. C. Yan, C. L. Brown and X. D. Yao, *Adv. Mater.*, 2016, **43**, 9532.
27 W. X. Yang, L. L. Chen, X. J. Liu, X. Y. Yue, C. Y. Liu and J. B. Jia, *J. Mater. Chem. A*, 2016, **4**, 5834.
28 S. B. Yang, L. J. Zhi, K. Tang, X. L. Feng, J. Maier and K. Müllen, *Adv. Funct. Mater.*, 2012, **22**, 3634.
29 W. H. Niu, L. G .Li, N. Wang, S. B. Zeng, J. Liu, D. K. Zhao and S. W. Chen, *J. Mater. Chem. A*, 2016, **4**, 10820.
30 G. L. Chai, Z. F. Hou, D. J. Shu, T. Ikeda and K. Terakura, *J. Am. Chem. Soc.*, 2014, **136**, 13629.
31 I. Y. Jeon, H. J. Choi, S. M. Jung, J. M. Seo, M. J. Kim, L. M. Dai and J. B. Baek, *J. Am. Chem. Soc.*, 2012, **135**, 1386.
32 W. Wei, Y. Tao, F. Y. Su, L. Ke, J. Li, D. W. Wang, B. H. Li, F. Y. Kang and Q. H. Yang, *Sci. Rep.*, 2014, **4**, 6289.
33 L. Hao, S. S. Zhang, R. J. Liu, J. Liu, J. Ning, G. J. Zhang and L. J. Zhi, *Adv. Mater.*, 2015, **27**, 3190.
34 Y. F. Zhao, S. F. Huang, M. R. Xia, S. Rehman, S. C. Mu, Z. K. Kou, Z. Zhang, Z. Y. Chen, F. M. Gao and Y. L. Hou, *Nano Energy*, 2016, **28**, 346.
35 I. Y. Jeon, Y. R. Shin, G. J. Sohn, H. J. Choi, S. Y. Bae, J. Mahmood, S. M. Jung, J. M. Seo, M. J. Kim, D. W. Chang, L. M. Dai and J. B. Baek, *Proc. Natl. Acad. Sci. U.S.A.*, 2012, **109**, 5588.
36 Y. P. Liu, L. Yuan, M. Yang, Y. Zheng, L. J. Li, L. B. Gao, N. Nerngchamnong, C. T. Nai, C. S. S. Sangeeth, Y. P. Feng, C. A. Nijhuis and K. P. Loh, *Nat. Commun.*, 2014, **5**, 5461.
37 A. Ranganathan, V. R. Pedireddi and C. N. R. Rao, *J. Am. Chem. Soc.*, 1999, **121**, 1752.
38 L. L. Feng, Y. C. Zou, C. G. Li, S. Gao, L. J. Zhou, Q. S. Sun, M. H. Fan, H. J. Wang, D. J. Wang, G. D. Li and X. X. Zou, *Int. J. Hydrogen. Energ.*, 2014, **39**, 15373.
39 F. Gao, J. Y. Qu, Z. B. Zhao, Q. Zhou, B. B. Li and J. S. Qiu, *Carbon*, 2014, **80**, 640.
40 W. Gao, L. B. Alemany, L. Ci and P. M. Ajayan, *Nat. Chem.*, 2009, **1**, 403.
41 X. L. Li, X. R. Wang, L. Zhang, S. Lee and H. J. Dai, *Science*, 2008, **319**, 1229.
42 L. J. Cote, F. Kim and J. Huang, *J. Am. Chem. Soc.*, 2009, **131**, 1043.
43 H. Hu, Z. B Zhao, W. Wan, Y. Gogosti and J. Qiu, *Adv. Mater.*, 2013, **25**, 2219.
44 S. N. Bhange, S. M. Unni and S. Kurungot, *J. Mater. Chem. A*, 2016, **4**, 6014.
45 S. Q. Peng, H. M. Jiang, Y. M. Zhang, L. Yang, S. Q. Wang, W. F. Deng, and Y. M. Tan, *J. Mater. Chem. A*, 2016, **4**, 3678.
46 W. W. Zhou, J. X. Zhu, C. W. Cheng, J. P. Liu, H. P. Yang, C. X. Cong, C. Guan, X. T. Jia, H. J. Fan, Q. Y. Yan, C. M. Li and T. Yu, *Energy Environ. Sci.*, 2011, **4**, 4954.
47 W. Ai, Z. Z. Du, Z. X. Fan, J. Jiang, Y. L. Wang, H. Zhang, L. H. Xie, W. Huang and T. Yu, *Carbon*, 2014, **76**, 148.
48 J. Z. Shang, L. Ma, J. W. Li, W. Ai, T. Yu and G. G. Gurzadyan, *Sci. Rep.*, 2012, **2**, 792.
49 C. Nethravathi and M. Rajamathi, *Carbon*, 2008, **46**, 1994.
50 Z. S. Wu , W. C. Ren, L. Xu, F. Li and H. M. Cheng, *ACS Nano*, 2011, **5**, 5463.
51 P. Li, J. Y. Liu, Y. W. Wang, Y. Liu, X. N. Wang, K. W. Nam, Y. M. Kang, M.B. Wu and J. S. Qiu, *Chem. Eng. J.*, 2016, **286**, 632.
52 C. G. Xu, G. Q. Ning, X. Zhu, G. Wang, X. F. Liu, J. S. Gao, Q. Zhang, W. Z. Qian and F. Wei, Carbon, 2013, **62**, 213.
53 G. Wu, N. H. Mack, W. Gao, S. G. Ma, R. Q. Zhong, J.T. Han, J. K. Baldwin and P. Zelenay, *ACS Nano*, 2012, **6**, 9764.
54 J. T. Zhang and L. M. Dai, *Angew. Chem. Int. Ed.*, 2016, **55**, 13296.
55 B. Men, Y. Z. Sun, M. J. Li, C. Q. Hu, M. Zhang, L. N. Wang, Y. Tang, Y. M. Chen, P. Wan and J. Q. Pan, *ACS Appl. Mater. Interfaces*, 2016, **8**, 1415.

View Article Online
DOI: 10.1039/C7TA03264A

56 J. Wei, Y. X. Hu, Y. Liang, B. Kong, J. Zhang, J. C. Song, Q. L. Bao, G. P. Simon, S. P. Jiang and H. T. Wang, *Adv. Funct. Mater.*, 2015, **25**, 5768.

DOI: 10.1039/C7TA03264A

Journal Name

COMMUNICATION

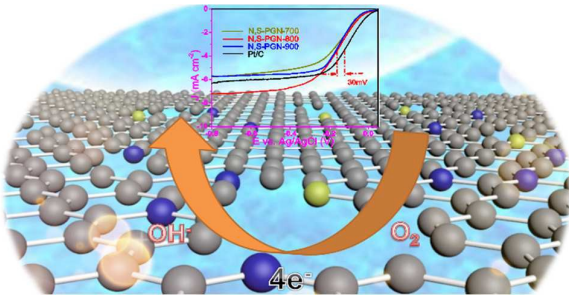

Supramolecular polymer-assisted synthesis of nitrogen, sulfur-codoped porous graphene networks (N,S-PGN) from petroleum coke for remarkable electrocatalytic activities for ORR.